Aggregation induced emission enhancement from antipyrine-based schiff base and its selective sensing towards picric acid

5.1. Introduction

Various organic luminescent materials have received a great deal of attention because of their potential applications in chemistry, materials science and biology [241-245]. Many luminogenic organic emitters are highly emissive in their dilute solution but their emissive property disappeared hastily in aggregated form [246, 247]. This phenomenon is notoriously known as Aggregation Caused Quenching (ACQ) effect. On the other hand, many luminescent materials are non-emissive in good solvent but they become emissive in their aggregated form. This phenomenon is called aggregation induced emission (AIE) effect [248, 249]. There are another class of molecules which are weakly emissive in good solvent but show strong emission in their aggregated state and the phenomenon is known as aggregation induced emission enhancement (AIEE) [250-254]. This unique characteristic differentiates them from conventional luminophores and focused on the exploration of their utilities in the development of optical sensors and other important applications. Fluorophores with AIEE characteristics have been successfully utilized in organic light emitting diodes (OLEDs) [255-257], photoemitters [258], electroluminescent materials [259], sensors [260-263], etc. Their mechanisms of action are usually explained in terms of, restriction of intermolecular rotation (RIR) [264], formation of excited-state proton transfer [265], intramolecular charge-transfer (ICT) [266,267], intramolecular hydrogen bond [268] etc.

Much attempt has been made to synthesize organic nano/ micro particles having various shapes and sizes. This includes zero dimensional (0-D) tetrahedral or spherical quantum dots [269], three-dimensional (3-D) cubic symmetry [270], two-dimensional (2-D) nanoplates [271], one-dimensional (1-D) nanorods and wires from small organic compounds [272, 273]. Diverse techniques were developed to prepare organic nano/micro particles, such as ultra-sonication [274], self-organization [275-277], microemulsion [278], template method [279], physical vapour deposition [280], reprecipitation [281], chemical reactions [282-285] etc. Among the aforesaid methods, reprecipitation is one of the most favoured routes towards the cost-effective large-scale production of nano/micro building blocks.

Due to mechanistic simplicity, high selectivity and sensitivity, fluorescent chemo-sensors have found potential applications in the detection of environmentally important analytes such as polynitroaromatic (PNAC) explosives. However, picric acid (PA) has also emerged as a potential substitute due to its high explosive power. In addition,

because it is highly soluble in water, PA is a major contaminant of groundwater. It is extensively used in the rocket fuel manufacturing, dye industry and pharmaceutical industry [286, 287]. PA is a non-biodegradable environmental pollutant, which causes several problems to human health, such as skin allergy, skin irritation and respiratory system and liver damage [288] etc. Thus, for social and environmental safety, effective monitoring and detection of trace amounts of PA, both in solution and vapor phase, is quite important. Physical detection methods for explosives include gas chromatography coupled with energy-dispersive X-ray diffraction [289], surface enhanced Raman spectroscopy [290], mass spectrometry [291], nuclear quadruple resonance spectroscopy [292] etc. These techniques are highly selective, but relatively complex and involve expensive instrumentation. Most detection methods for explosives are only applicable to vapor samples because of interference problems encountered in complex aqueous media. Thus the development of a fast and selective method for the detection of PA in aqueous medium is highly desirable [293-295].

Here, we have introduced a Schiff base, 4-[(2-Hydroxy-naphthalen-1-ylmethylene)-amino]-1,5-dimethyl-2-phenyl-1,2-dihydro-pyrazol-3-one [**P^3**], where free rotating groups antipyrine and hydroxy naphthalene moieties are attached to the azo group. Aggregated **P^3** exhibits AIEE effect and strong green fluorescence is observed under ultraviolet irradiation. Microstructures of **P^3** with various morphologies have been synthesized using SDS as morphology directing agent. Morphologies of the particles were characterized using optical and scanning electron microscopy (SEM). The turn off luminescent property of aggregated **P^3** hydrosol in presence of PA is used for the selective detection of trace amounts of picric acid (PA) in aqueous medium. The fluorescence quenching of the hydrosol in the presence of PA has been explained due to the ground state complexation between **P^3** and PA.

5.2. Experimental section

5.2.1. Materials

2-hydroxy-1-naphthaldehyde was purchased from Sigma-Aldrich Chemical Corp. 4-aminoantipyrine was purchased from Merck India Ltd. All the solvents used were of analytical grade. Sodium dodecyl sulphate (SDS) was purchased from Merck India Ltd. and was recrystalized from 1:1 ethanol water mixture. Picric acid (PA), dinitro benzene (DNB), 4-nitrophenol (NP), 3, 5-dinitrobenzoic acid (3, 5-DNBA), 2, 4-dinitrophenol (DNP) and 2, 4-dinitro toluene (DNT) were purchased from E-Merck India Ltd. The purity of these chemicals was checked spectrophotometrically. Triply distilled deionized water was used throughout the experiments.

5.2.2. Synthesis of P^3 and P^3-Microparticles

2-hydroxy-1-naphthaldehyde (1 equiv) was added to 1 equiv of 4-aminoantipyrine in 50 mL of methanol with constant stirring and then refluxed for 10 h. The reaction was monitored by thin-layer chromatography. After completion, the reaction mixture was cooled, and bright yellow color crystalline solid product was filtered and washed thoroughly with methanol and then dried in a desiccators. Yield: 80%. Anal. Calcd for $C_{22}H_{19}N_3O_2$: C, 73.93%; H, 5.36%; N, 11.76%; Found: C, 73.82%; H, 5.24%; N, 11.59%. FT-IR (KBr), ν, cm^{-1}: 3426 (O − H), 1637 (C = 0), 1586 (C = N), 1478 (C = C), 1143 (N − N). ^{1}H NMR (400 MHz, $CDCl_3$, δ (ppm)) δ: 2.49 (3H, s), 3.23 (3H, s), 8.28−7.17 (11H, ArH), 10.85 (1H, s); ^{13}C NMR (100 MHz, $CDCl_3$, δ (ppm)) δ: 10.31, 35.69, 110.60, 116.36, 119.51, 120.55, 123.38, 124.62, 127.35, 127.57, 127.87, 128.84, 129.35, 132.83, 133.68, 134.33, 149.07, 156.77, 160.50, 162.16 ppm. The microstructures of **P^3** were prepared by re-precipitation method and SDS was used as morphology directing agent. In a typical preparation, small volume of 1mM **P^3** in MeOH was injected into 5 mL of continuously stirred water and aqueous SDS separately at room temperature (25°C) for 5 min. Clearness of the solution gradually decreased with increasing concentration of **P^3** and a milky greenish color was appeared. The solution was allowed to stand for overnight. Volume of **P^3** and concentration of SDS were varied to synthesize various microstructures of **P^3**. During the synthesis of sample-a, b, c, d, e, f, & g concentration of SDS (3.96 mM) were kept constant and the concentration of **P^3** (sample-a: 1.9μM, sample-b: 9.9μM, sample-c: 19.6μM, sample-d: 38.4μM, sample-e: 56.6μM, sample-f: 74μM, sample-g: 90.9μM, sample-h: 166.6μM) was varied in order to study the effect of concentration of **P^3** on aggregated structures. Similar method was used for the preparation of **P^3** microstructures in the absence of SDS and the samples are named as sample-a_1 to h_1 respectively.

Scheme 5.1: Synthesis of 4-[(2-Hydroxy-naphthalen-1-ylmethylene)-amino]-1,5-dimethyl-2-phenyl-1,2-dihydro-pyrazol-3-one (**P^3**)

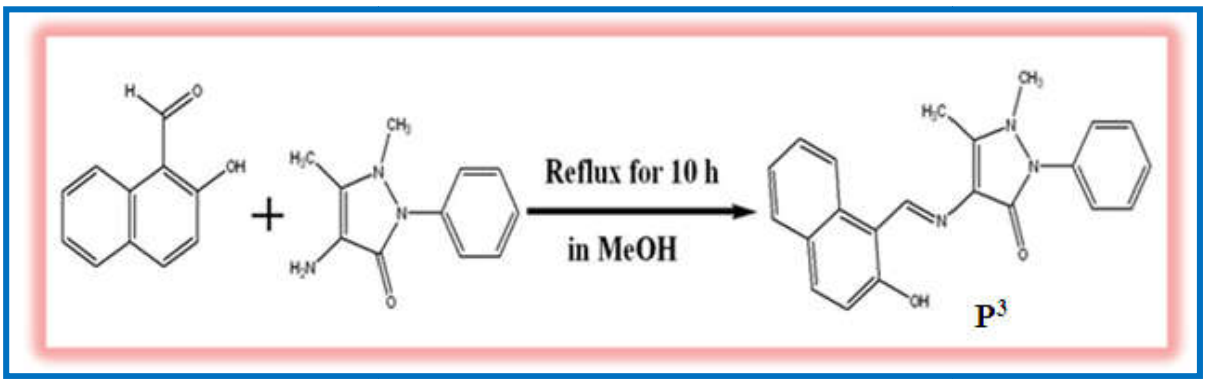

5.2.3. Characterization

UV-Vis spectroscopic measurements were carried out in a 1cm quartz cuvette with a Shimadzu UV-1800 spectrophotometer. Fluorescence spectra were recorded using Hitachi F-7000 Fluorescence Spectrophotometer. NMR spectra were recorded on a Bruker ASCEND spectrometer in $CDCl_3$. The Fourier transform infrared (FT-IR) spectra were obtained in the range of 4000−400 cm^{-1} using KBr pellets on a PerkinElmer Spectrum-Two FTIR spectrometer. The Morphologies of the synthesized nano/microstructures were studied using a ZEISS EVO 18 Scanning Electron Microscope (SEM) with an accelerating voltage of 5 kV. Samples for the SEM study were prepared by placing a drop of the aqueous suspension of particles on a small glass slide followed by solvent evaporation under vacuum. To minimize sample charging, the dried samples were coated with a thin gold layer right before SEM study. Time-resolved fluorescence measurements were carried out under ambient conditions using a time-correlated single-photon counting (TCSPC) spectrometer [a picosecond diode laser (IBH, UK)] with the detection wavelength at 500 nm for **P^3**. Excitation wavelength was 402 nm for all the samples. Lamp profiles were measured with a band-pass of 3 nm using Ludox as the scatterer. The decay parameters were recovered using non-linear iterative fitting procedure based on the Marquardt algorithm [296]. The quality of fit was assessed over the entire decay, including the rising edge, and tested with a plot of weighted residuals and other statistical parameters e.g. the reduced $\chi 2$ ratio [297]. The signal was detected at magic angle (54.7°) polarization using a Hamamatsu MCP PMT (3809U). Time resolution of the experimental setup was ~90 ps. Optical microscopy images were taken using an NIKON ECLIPSE LV100POL upright microscope equipped with CCD camera (model no. Nikon DS-Fi l), polarizer-analyzer assembly and 100W mercury lamp as excitation source for emission study. The samples for optical microscopic study were prepared by placing a drop of colloidal solution onto a clean glass slide. XRD was recorded in a 'Rigaku Miniflex-II' X-ray diffractometer using CuKα radiation (λ = 0.154056 nm). Scans were collected on powder samples in the range of 5°–80°.

5.2.4. Detection Limit

The detection limit was calculated on the basis of the fluorescence titration. The fluorescence emission spectrum of **P^3** as a function of its increasing concentration was measured five times, and the standard deviation (σ) of blank measurement was calculated. To obtain the slope (k), the fluorescence emission intensity at 500 nm was plotted against the concentration of PA. The detection limit was calculated using the following equation [298].

$$\text{Detection limit} = 3\sigma/k$$

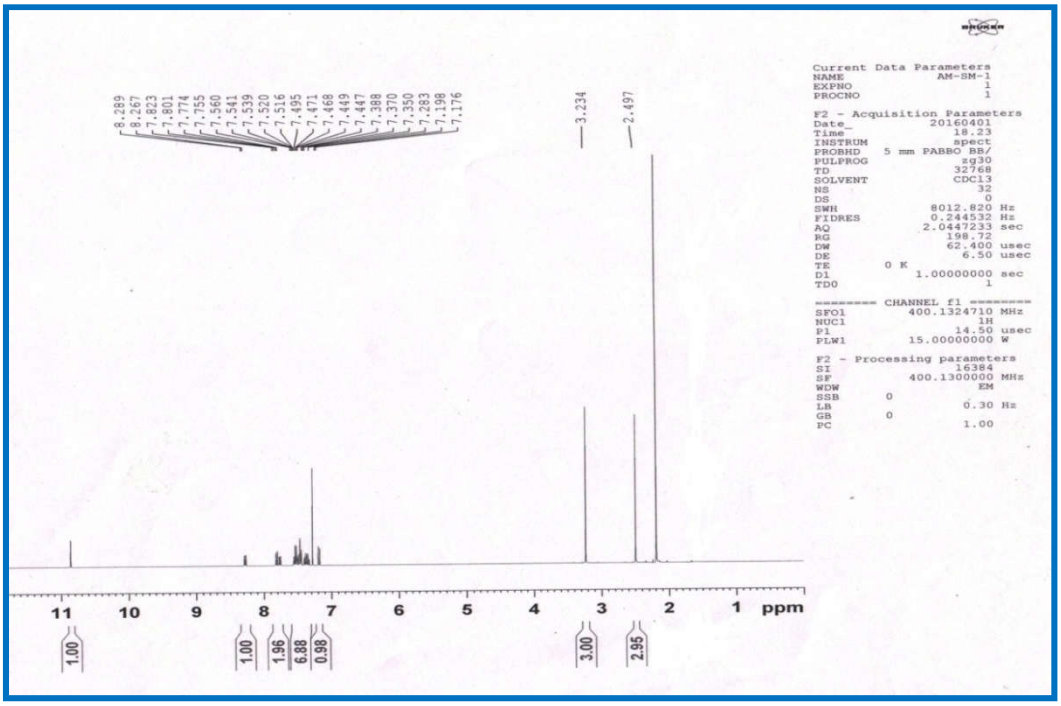

Fig. 5.1: ^{1}H NMR spectra of $\mathbf{P^3}$ in $CDCl_3$.

5.3. Results and discussion

Synthesis of $\mathbf{P^3}$ is depicted in ***Scheme 5.1*** and synthesis details are described in Experimental Section. It was completely characterized by physicochemical and spectroscopic analysis. The ^{1}H NMR (***Fig. 5.1***) and ^{13}C NMR (***Fig. 5.2***) spectra were recorded to confirm the purity and the structure of the probe. IR (***Fig. 5.3***) spectrum shows a vibration band at 1586 cm^{-1} which can be assigned to stretching vibrational mode of imine (−CH=N−) groups in the $\mathbf{P^3}$ molecules. Powder XRD (***Fig. 5.4***) study confirms the purity of the as-prepared particles of $\mathbf{P^3}$

5.3.1. SEM study

Scanning electron microscopic (SEM) study of the aggregated hydrosol with increasing concentration of $\mathbf{P^3}$ for a fixed SDS concentration (4 mM) are shown as sample-c, e, g & h in ***Fig. 5.5.*** Morphology of the aggregated particle is rectangular plate like at low concentration of $\mathbf{P^3}$. On the other hand, morphology of the particle changes from rectangular plate to wire with increasing concentration of $\mathbf{P^3}$ and there is a clear indication that dimension of the particles decreases in one direction with the increasing concentration of $\mathbf{P^3}$. We have also synthesized $\mathbf{P^3}$ microstructures in the absence of SDS using identical experimental conditions.

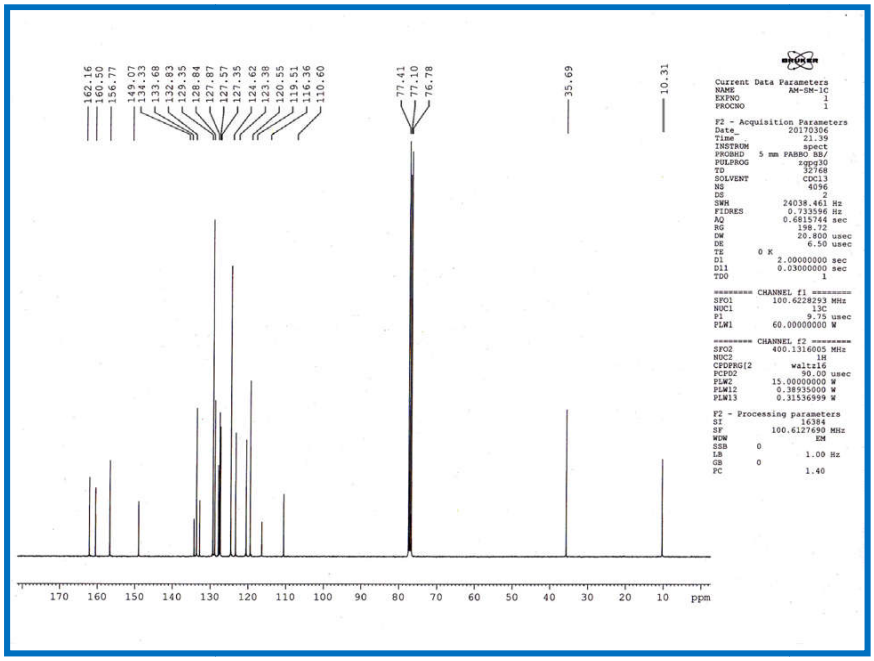

Fig. 5.2: ^{13}C NMR spectra of **P^3** in $CDCl_3$.

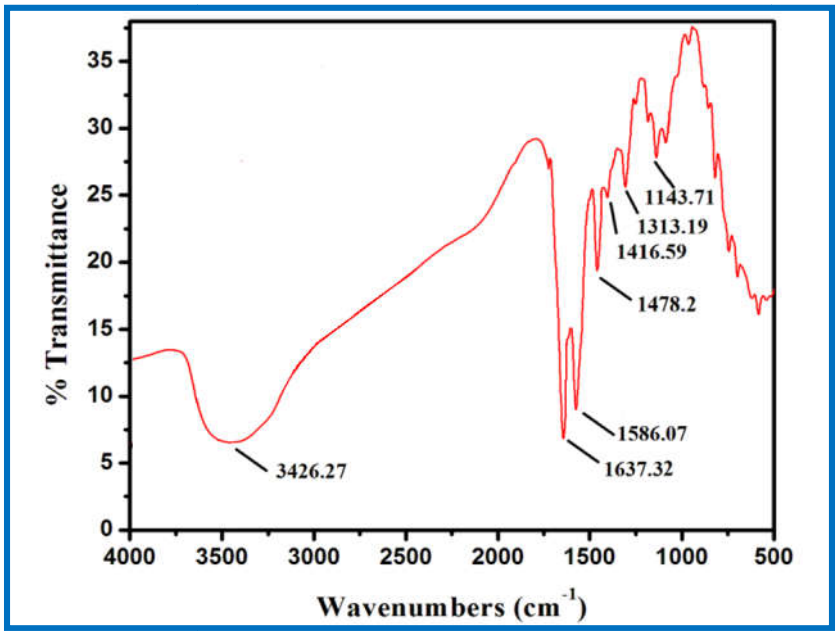

Fig. 5.3: FT-IR spectra of **P^3** showing sharp peak at 1586 cm^{-1} for C=N bond, 3426 cm^{-1} (O − H), 1637 cm^{-1} (C = 0), 1478 cm^{-1} (C = C), 1143 cm^{-1} (N − N).

In the absence of SDS, wire like microstructures with reduced thickness are obtained at low concentration of **P^3** and the thickness of wire increases as the concentration of **P^3** increases and this is in contrast with morphology of the particle in the presence of SDS (***Fig. 5.6***). Here, the concentration of SDS (4 mM) used is almost half than its CMC value. There are some early reports that the CMC of SDS decreases with the added impurities in the solution [299]. It seems that **P^3** acts as impurity to reduce the CMC value of SDS. Thus at

higher P^3 concentration the CMC of SDS is reduced to such an extent that SDS starts to form micelle. Now the hydrophobic core of micelle act as good solvent for P^3 and more and more P^3 get solubilised within the miceller core. Therefore the effective concentration of P^3 to form micro aggregates is decreased and it results microcrystals with reduced thickness in presence of SDS at this higher concentration of P^3.

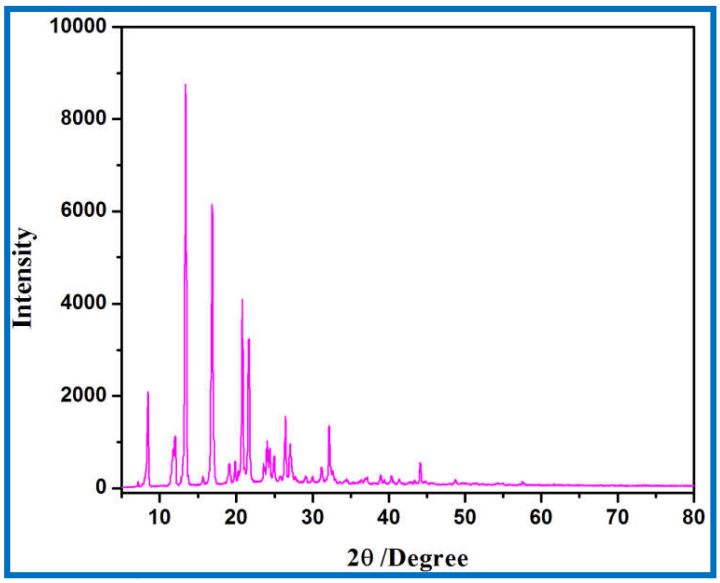

Fig. 5.4: Powder XRD spectra of P^3.

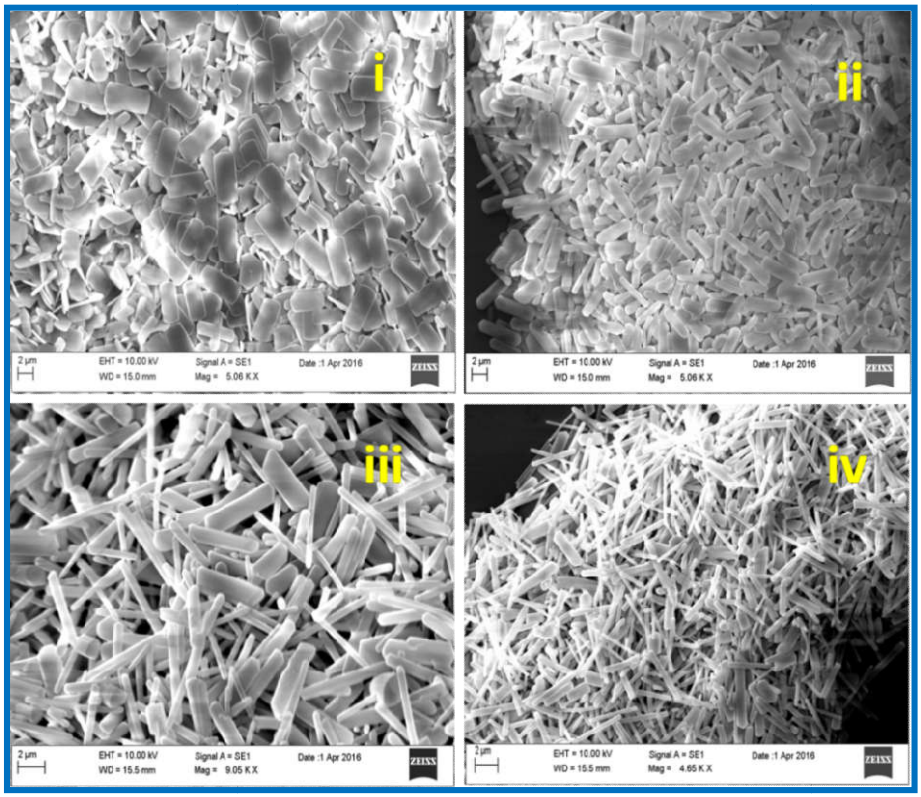

Fig. 5.5: SEM images of P^3 microstructures prepared in presence of 4 mM SDS (i) sample-c, (ii) sample-e, (iii) sample-g, (iv) sample-h.

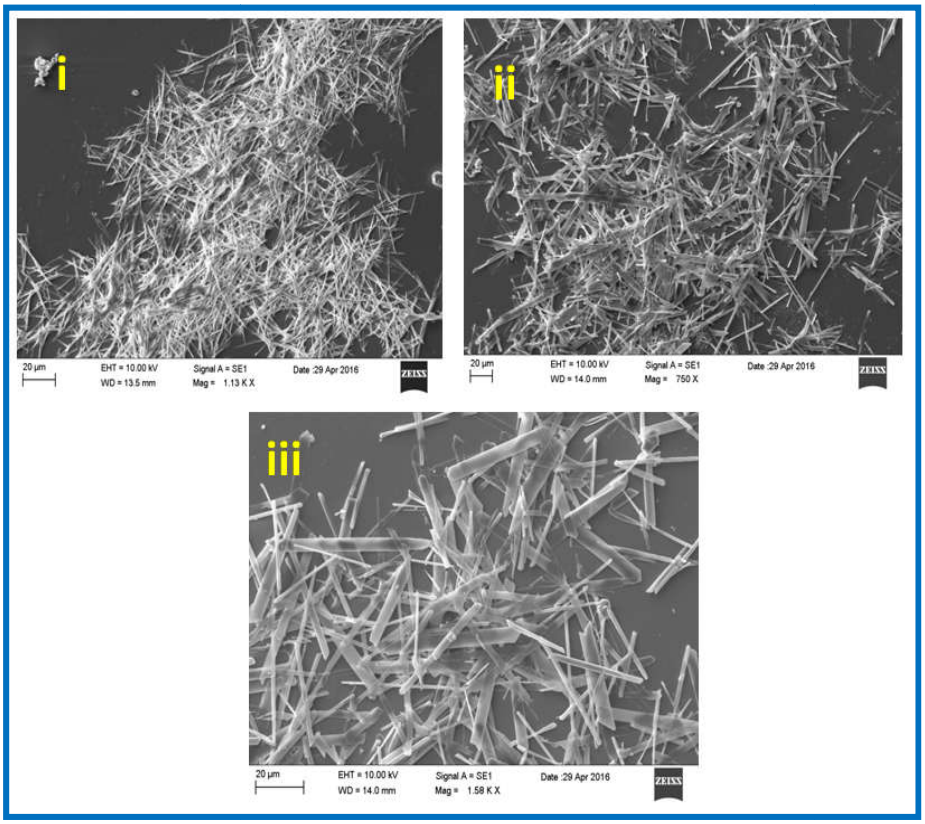

Fig. 5.6: SEM images of $\mathbf{P^3}$ microstructures prepared in the absence of SDS (i) sample-c_1, (ii) sample-e_1, (iii) sample-h_1.

5.3.2. Optical microscopic study

Morphologies of the particles as observed by fluorescence microscopy are in consistent with its SEM images (***Fig. 5.7***). Wire shaped morphologies at a lower concentration of $\mathbf{P^3}$ are clearly observed for the sample-c, e, g, h using optical microscopy. Regular one dimensional growth of the microcrystals is observed with increasing concentration of $\mathbf{P^3}$. $\mathbf{P^3}$ shows rod-shaped microstructures with greenish sky emission upon UV excitation. There is a clear indication that dimension of the particles increases along its length and decreases along the breadth with increasing concentration of $\mathbf{P^3}$. Like SEM images, similar optical images of $\mathbf{P^3}$ microstructures are obtained with greenish sky emission upon UV excitation in the absence of SDS. Glittering light emissions are observed at the ends of the microcrystals (***Fig. 5.8***), indicating that optical waveguide effect is operating in the light transmission process within the microcrystals.

5.3.3. UV-Vis Study

UV–Vis absorption spectra of $\mathbf{P^3}$ in MeOH and the as prepared hydrosol of $\mathbf{P^3}$ (sample a, b, c, d, e, f, g) are shown in ***Fig. 5.9***. The UV–Vis absorption spectrum of $\mathbf{P^3}$ in MeOH has two distinct region at 425-475 nm and 420-320 nm respectively.

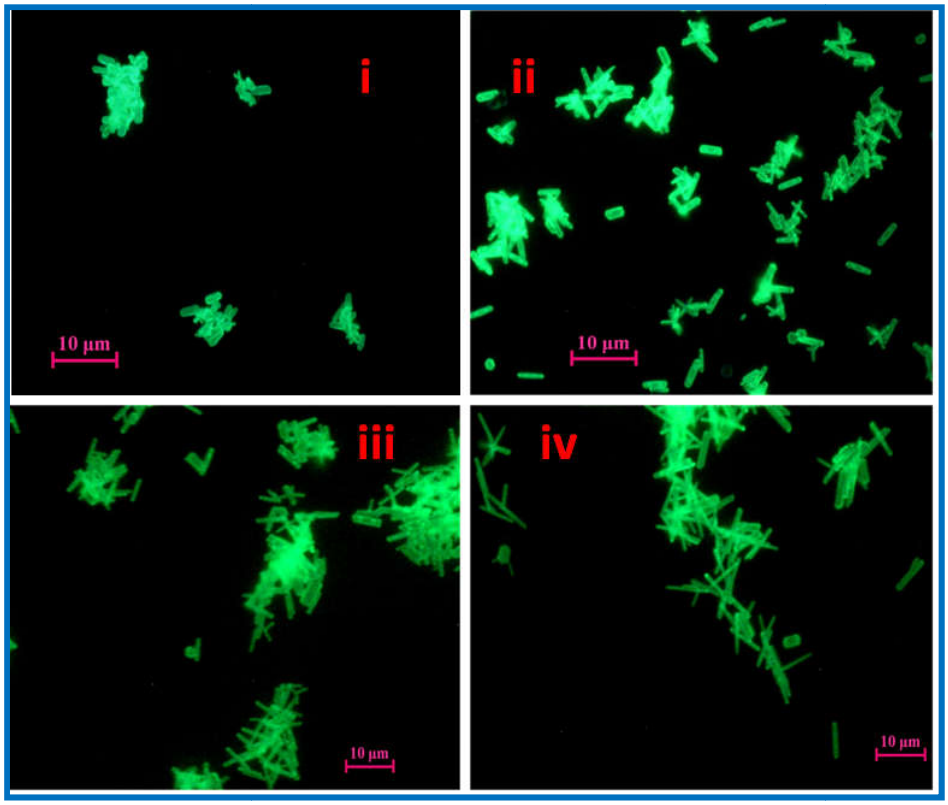

Fig. 5.7: Optical fluorescence microscopy images (under UV excitation) of $\mathbf{P^3}$ microstructure prepared in presence of 4 mM SDS (i) sample-c, (ii) sample-e (iii) sample-g (iv) sample-h.

Both the bands are different from either of the aromatic antipyrine and naphthalene moieties present in $\mathbf{P^3}$. A comparison of UV-Vis spectra of $\mathbf{P^3}$ with that of antipyrine and naphthalene moieties (***Fig. 5.10***) suggests that the band at 420-320 nm is due to perturb π–π* transition of 2-hydroxy-1-naphthaldehyde. On the other hand, the effect of solvent polarity on the UV-Vis spectra shows that the band at 425-475 nm is red shifted and decreased in intensity with increasing polarity of the solvent (***Fig. 5.11***). Therefore the red shifted weak and broad absorption band at 425-475 nm is due to charge transfer transition between naphtaldehyde and antipyrine moiety present in $\mathbf{P^3}$.

However, with increasing water fraction, the aggregate begin to form, and the maximum absorption peak at 382 nm diminishes (***Fig. 5.9***). Meanwhile, a new shoulder band is appeared at around 432 nm and the absorbance of the band increases with increasing water fraction. It is discussed previously that $\mathbf{P^3}$ shows a weak CT band in solution. Now with increased water fraction in the solution $\mathbf{P^3}$ starts to form aggregates and the weak CT band become intense due to increased concentration of charge transfer excitons in the aggregated state. On the other hand the CT excitons faces less polar environment within the aggregates compare to solution state and thus shows a blue shift with increasing fraction of water. In addition, the overall shift of the spectral baseline of samples a-g relative to that of the

monomer is attributed to the scattering of light by the larger aggregated structures in solution (***Fig. 5.12***).

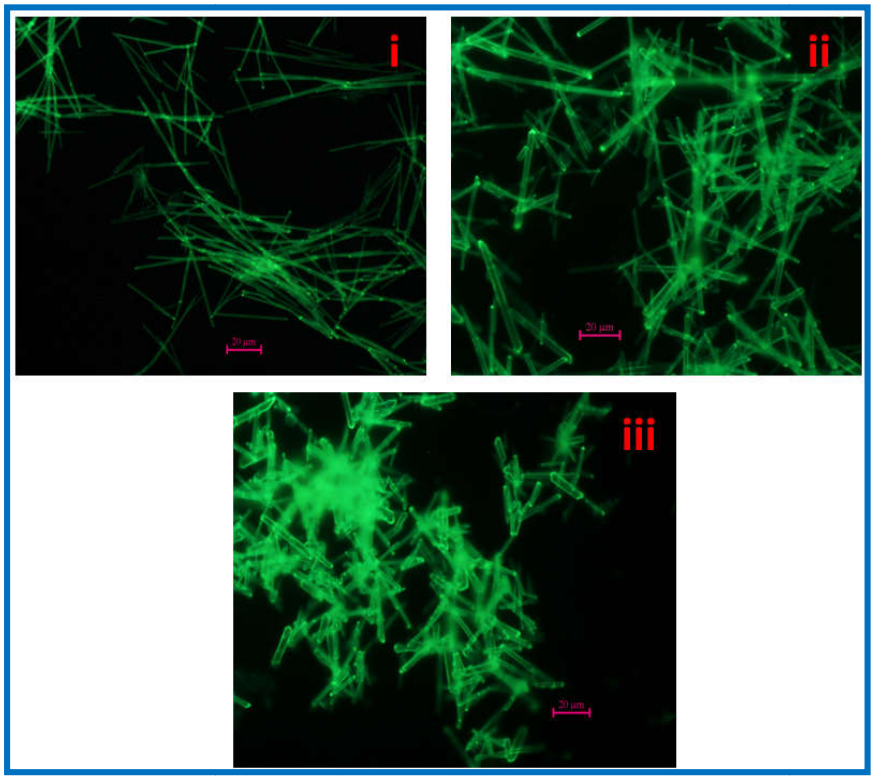

Fig. 5.8: Optical fluorescence microscopy images (under UV excitation) of aggregated microstructures prepared in the absence of SDS (i) sample-c1, (ii) sample-e1 (iii) sample-h1.

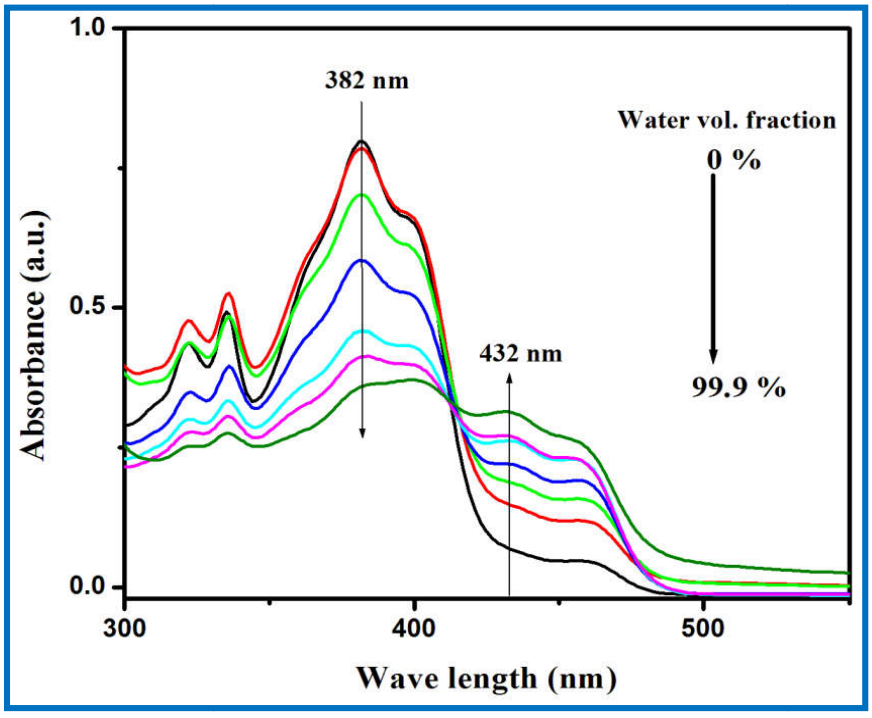

Fig. 5.9: UV-Vis absorption spectra of $\mathbf{P^3}$ in (i) 0% water ($\mathbf{P^3}$ in MeOH), (ii) 20% water, (iii) 40% water, (iv) 80% water, (v) 90% water and (vi) 99.9% water.

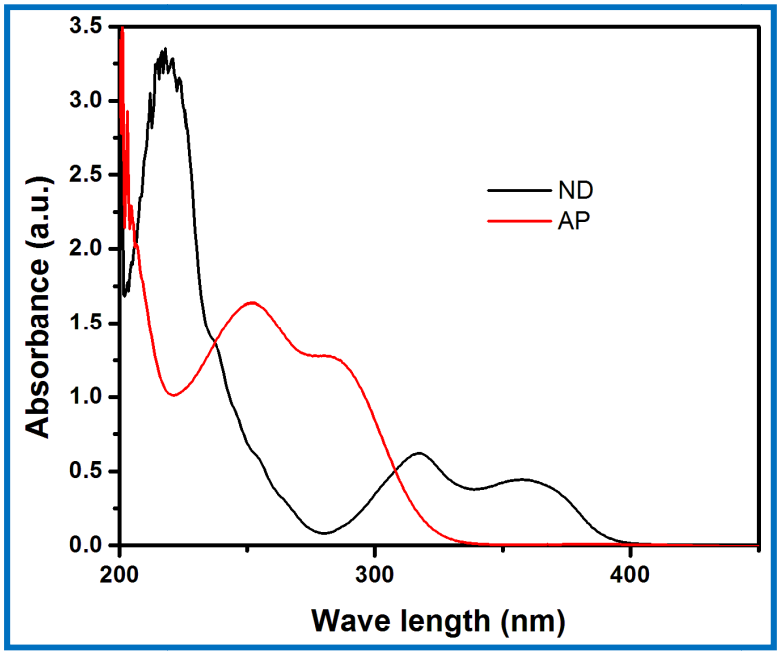

Fig. 5.10: UV-Vis spectra of 2-hydroxy-1-naphthaldehyde and 4-aminoantipyrine in MeOH.

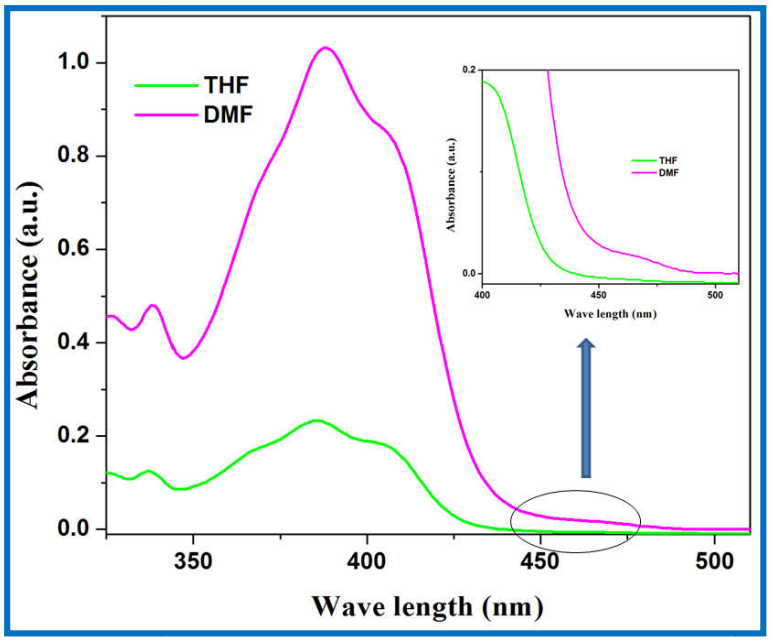

Fig. 5.11: UV-Vis spectra of NDAP in different solvent polarity.

5.3.4. Emission Study

PL spectra of **P**^{3} in MeOH and its aggregated hydrosol with different amount of **P**^{3} are shown in (***Fig. 5.13a***). It is observed that the dilute solution (6 μM) of **P**^{3} in MeOH exhibits very weak structured emission with peaks at 440, 473 and 482 nm respectively upon photoexcitation at 410 nm. But the aggregated hydrosol of **P**^{3} exhibits nearly 27 nm red shifted intense structured emission with a maximum at 500 nm. It is also observed that PL

intensity of P^3 hydrosol in the region 450-600 nm increases gradually compare to P^3 in MeOH with increasing concentration of P^3.

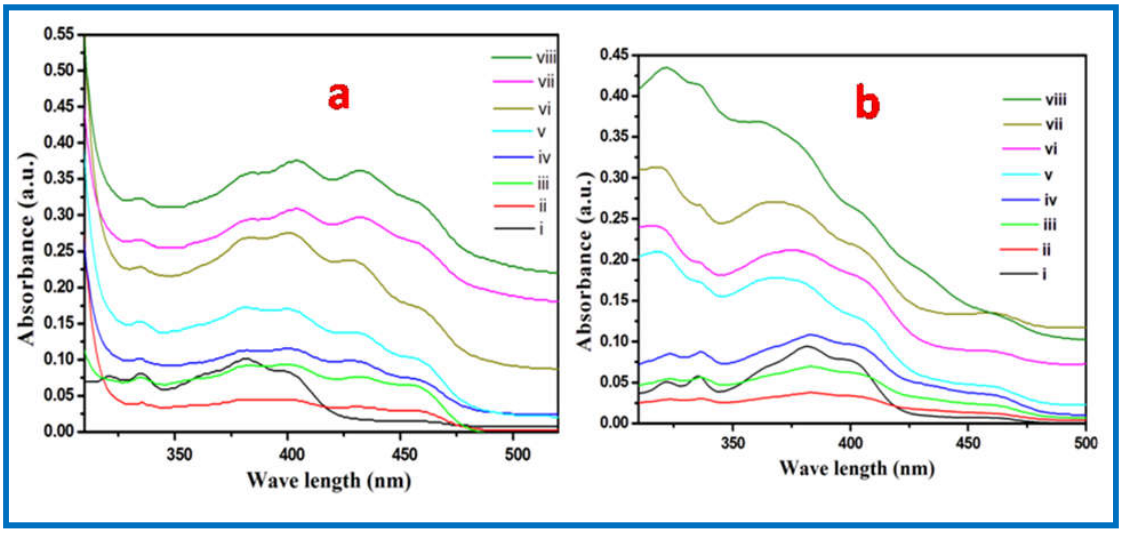

Fig. 5.12: a) UV-Vis absorption spectra of (i) P^3 in MeOH; P^3 hydrosol prepared in the absence of SDS (ii) sample-a1, (iii) sample-b1, (iv) sample-c1, (v) sample-d1, (vi) sample-e1, (vii) sample-f1, , (viii) sample-g1, c) UV-Vis absorption spectra of P^3 hydrosol prepared in the presence of 4 mM SDS (i) P^3 in MeOH (ii) sample-a, (iii) sample-b, (iv) sample-c, (v) sample-d, (vi) sample-e, (vii) sample-f, (viii) sample-g.

This is due to aggregation induced emission enhancement (AIEE) effect and it reaches a maximum at 90.9 μM P^3 and then decreases with a further increase in P^3 concentration (***Fig. 5.13a***). Thus 90.9 μM is the optimum concentration of P^3 for the AIEE, below which aggregation of P^3 occurs in such a way that it can form emissive crystalline structures but further increase in concentration (166.6 μM), P^3 orients in a random fashion to soften the microcrystals and is responsible for decreased emission intensity of the hydrosol. Also a similar observation in PL study using different concentration of P^3 for a fixed volume of aqueous SDS is shown in ***Fig. 5.13b***. It shows that the PL intensity of the aggregated hydrosol of P^3 in SDS (4 mM) is lower compared to the hydrosol without SDS. Since micellar core act as good solvent for P^3 rather than to form aggregates, the AIEE process is less favoured in SDS.

Fig. 5.13c shows the fluorescence emission spectra of P^3 at different volume fractions of water for a fixed concentration of P^3 (62 μM). It is observed that PL intensity increases gradually up to 90% water fraction, indicating the superb AIEE properties of P^3. But a sharp change of PL spectra with increased intensity are observed as the volume percentage of water changes from 90% to 99%. PL spectrum of the aggregated hydrosol at 99% v/v is red shifted and it is due to strong perturbation of excited P^3 with other neighbouring P^3 in a more rigid

non polar crystalline environment. But at > 90% water fraction, the emission is purely appeared from the aggregated hydrosol of **P^3** under UV irradiation and is shown in the inset of ***Fig. 5.13d.***

5.3.5. DFT Study

We have optimized the ground state geometry of **P^3** (***Fig. 5.14a***) and also computed HOMO,LUMO electron density using density functional theory (DFT) with the B3LYP/6-31G (d, P) basis. We have used Gaussian 09 package program for computational study [300]. Our computed HOMO electron density (***Fig. 5.14b***) illustrates that electron densities are localized within 2-hydroxy naphthalene group. On the other hand, LUMO electron densities are localized to the pyrazolin ring of **P^3**. This clearly signifies that charge transfer from 2-hydroxy naphthalene group to pyrazolin group takes place in the excited state of **P^3**. It is also observed that the HOMO, LUMO energy gap of **P^3** (3.6654 eV) is lower than 2-hydroxy naphthalene (4.01eV) and Pyrazolin (4.74 eV) moieties (***Fig. 5.14b***). This lowering of HOMO-LUMO gap in **P^3** is due to conjugation of π-electron of antipyrine and 2-hydroxy naphtaldehyde in **P^3**.

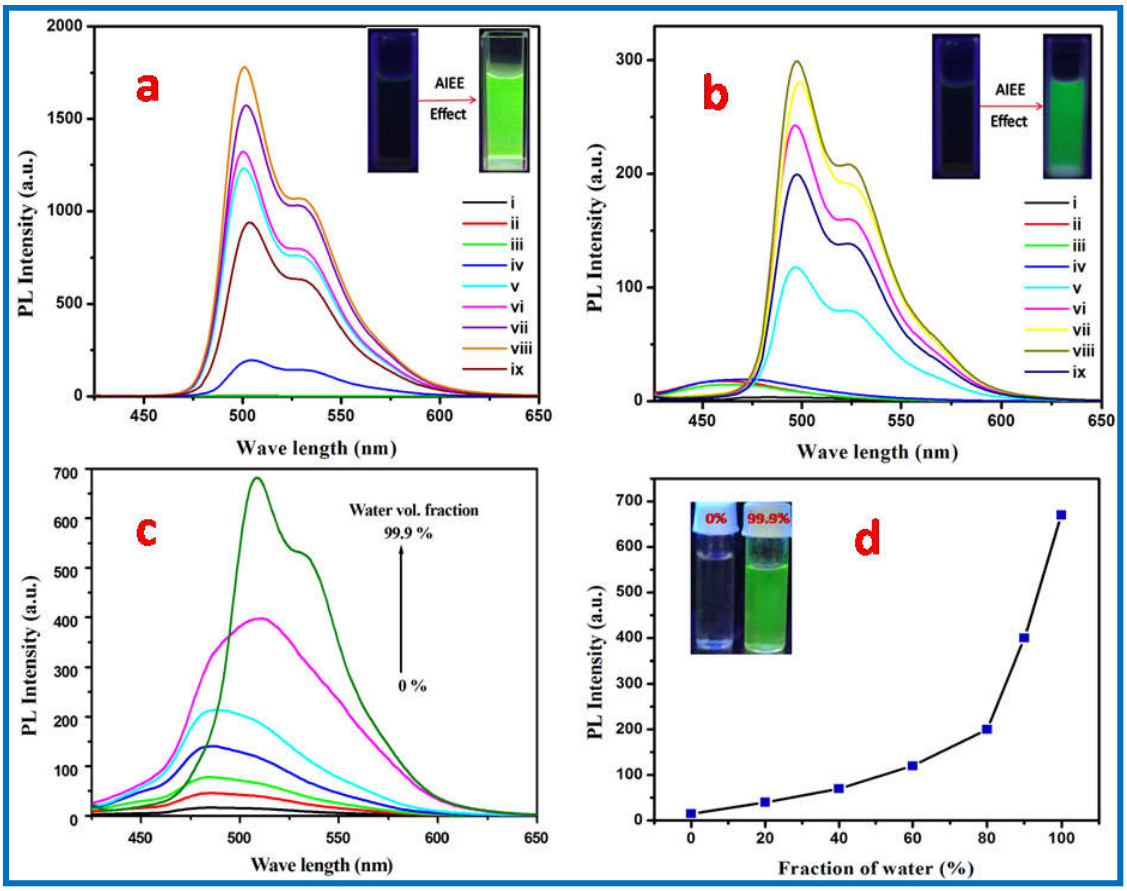

Fig. 5.13: (a) Fluorescence emission spectra of (i) **P^3** in MeOH, **P^3** hydrosol prepared in the absence of SDS (ii) sample-a1, (iii) sample-b1, (iv) sample-c1, (v) sample-d1, (vi) sample-e1,

(vii) sample-f1, (viii) sample-g1, (ix) sample-h1 (b) The Fluorescence emission spectra of **P³** hydrosol prepared in the presence of 4 mM SDS (i) **P³** in MeOH (ii) sample-a, (iii) sample-b, (iv) sample-c, (v) sample-d, (vi) sample-e, (vii) sample-f, (viii) sample-g, (ix) sample-h. All emission spectra were taken with 410 nm excitation. Inset Fluorescence images of **P³** in MeOH and its aggregated hydrosol under illumination of 366 nm radiation. (c) Emission spectra of freshly prepared **P³** (62 μM) in 0% -99.9% water. λex: 410 nm. (d) Plot of relative variation of PL intensity against water content (fw) in the MeOH/water mixture. Insets: Fluorescence images of **P³** (0% and 99% H2O) under 366 nm illuminations.

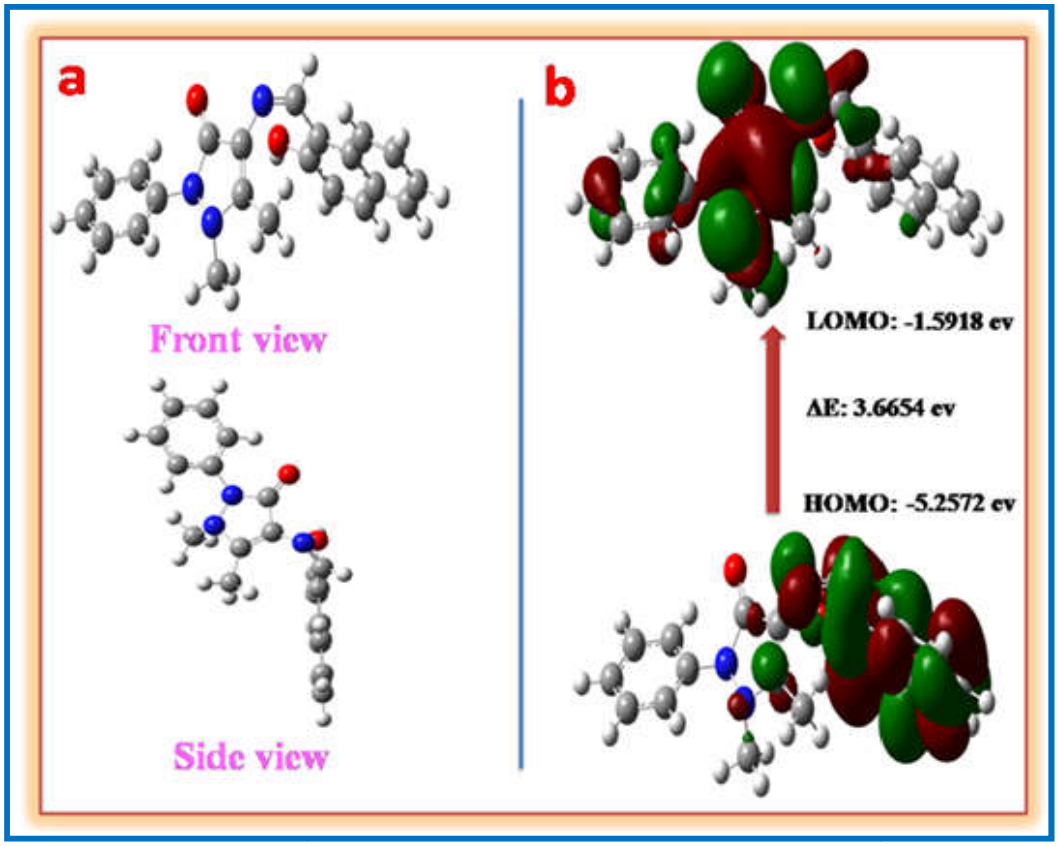

Fig. 5.14: a) Optimized structure of **P³**. b) Frontier molecular orbital plots of HOMO and LUMO energy levels of **P³** calculated by using DFT-B3LYP/6-31 G (d,p) level of theory as implemented on Gaussian 09.

5.3.6. Picric acid sensing

UV-Vis spectra of **P³** hydrosol in presence of picric acid (PA) shows that the CT band at 460 nm decreased and the absorption band~430 nm due to 2-hydroxy naphthalene moiety increases (***Fig. 5.15a***) . It seem electron deficient picric acid shows strong affinity towards electron rich antipyrine group of **P³**, resulting decreases in the absorption of CT band due to charge transfer between antipyrine and 2-hydroxy naphthalene group in **P³**. Thus the absorption band of the freed 2-hydroxy naphthalene group at~430 nm increases upon addition

of picric acid to the P^3 hydrosol. But, the addition of other nitroaromatic compounds to P^3 hydrosol does not show any detectable change in the absorption spectrum.

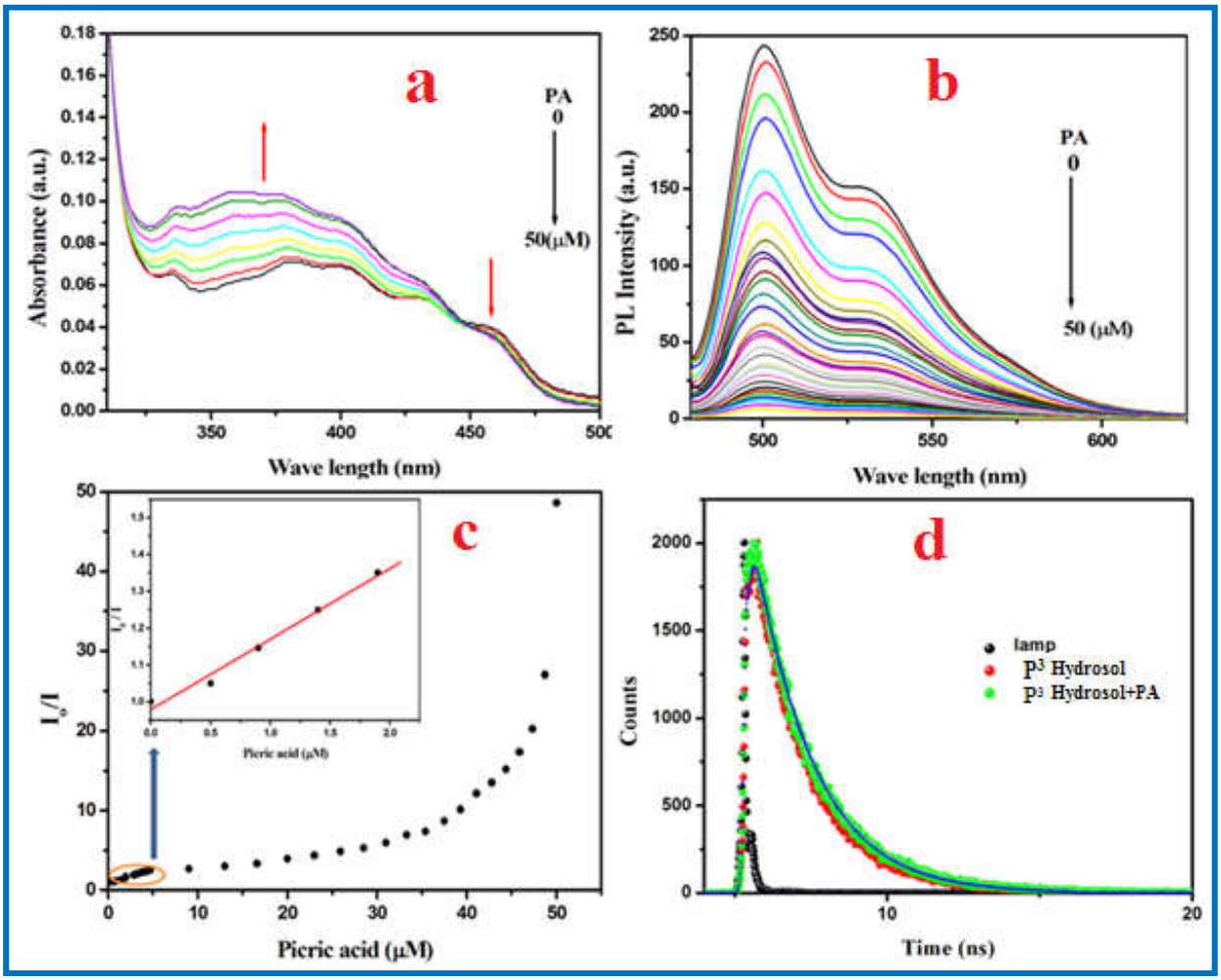

Fig. 5.15: (a) UV-Vis spectra and (b) Fluorescence emission spectra of P^3 hydrosol (sample-d) in presence of increasing concentration (0-50 μM) of PA in water. λex: 465 nm.(c) Plot of I0/I versus [PA] for P^3 hydrosol. (Inset: Linear variation of the plot in presence of increasing PA concentration) (d) Fluorescence lifetime of P^3 hydrosol in absence and presence of PA (λem: 500 nm and λex = 402 nm).

The fluorescence spectrum of P^3 hydrosol exhibits an intense emission peak at 500 nm (λex = 465 nm to avoid the inner filter effect due to increased concentration of PA in the solution). Upon gradual addition of PA to P^3 hydrosol, the emission intensity decreases, but the PL spectral position remains unchanged (***Fig. 5.15b***). The plot of I_0/I versus [PA] shows an upward curvature instead of linear relationship (inset of ***Fig. 5.15c***) indicating that quenching efficiency increases with increasing concentration of quencher. As the concentration of PA is below 3μM a linear Stern-Volmer plot is obtained with quenching constant value 1.91 x 10^5 M^{-1} which is found to be higher as compared to other reported

chemosensors for picric acid [301]. At a higher concentration of PA, the plot bent upward, indicating super amplified quenching effect [302].

Equation $I_0/I = 0 + 0.693e^{13.22[PA]}$ is obtained by fitting the concave curve of ***Fig. 5.15c***. From this equation, quantitative analysis can be realized. This strong fluorescence quenching of $\mathbf{P^3}$ hydrosol in presence of PA may be due to static /dynamic or combination of both static and dynamic quenching mechanism. This uncertainty is resolved by measuring fluorescence lifetime of $\mathbf{P^3}$ hydrosol in presence and absence of PA. Fluorescent decay curves of $\mathbf{P^3}$ hydrosol both in presence (1.91 ns) and absence of PA (1.82 ns) are fitted with single-exponential decay and this fitted components are almost similar for both the cases (***Fig. 5.15d***). This unchanged fluorescence lifetime of $\mathbf{P^3}$ hydrosol in the presence of PA suggests ground state complexation between $\mathbf{P^3}$ hydrosol and PA. Fluorescence quenching of $\mathbf{P^3}$ hydrosol in presence of different nitro aromatic compounds (PA, DNP, NP, DNT, DNBA, DNB) are also studied (***Fig. 5.16a***) and it is observed that the quenching efficiency of PA is much higher compare to other nitro aromatics (***Fig. 5.17 & Table 5.1***). Our measured quenching efficiency (%) by different nitroaromatics is shown in ***Fig. 5.16b***. We have carried out the anti-interference experiment to show the selective sensing property of $\mathbf{P^3}$ towards picric acid. A bar diagram showing fluorescence quenching of $\mathbf{P^3}$ by PA in presence of other nitroaromatics is shown in ***Fig. 5.18***. We further measure the limit of detection of PA using 3σ method and the detection limit is found to be 0.11 μM.

Fluorescence quenching was observed upon dipping the test strips into saturated aqueous solution of PA. For detection of very small amounts of PA, we prepared the aqueous PA hydrosol using different PA concentration and the hydrosol was placed on each test strip. The visual detection response of PA at different concentration is shown in ***Fig. 5.19***. The minimum amount of PA detectable by naked eye was up to 10^{-7} M level. Further, we prepared several samples of aggregated hydrosol filter papers and studied the response of their fluorescence toward picric acid in contact mode and solution phase as shown in ***Fig. 5.20***. PA crystals were placed over a test strip for 5 s to test the contact mode response of aggregated hydrosol toward PA. Upon illumination with UV lamp, black spots were observed in the contact area.

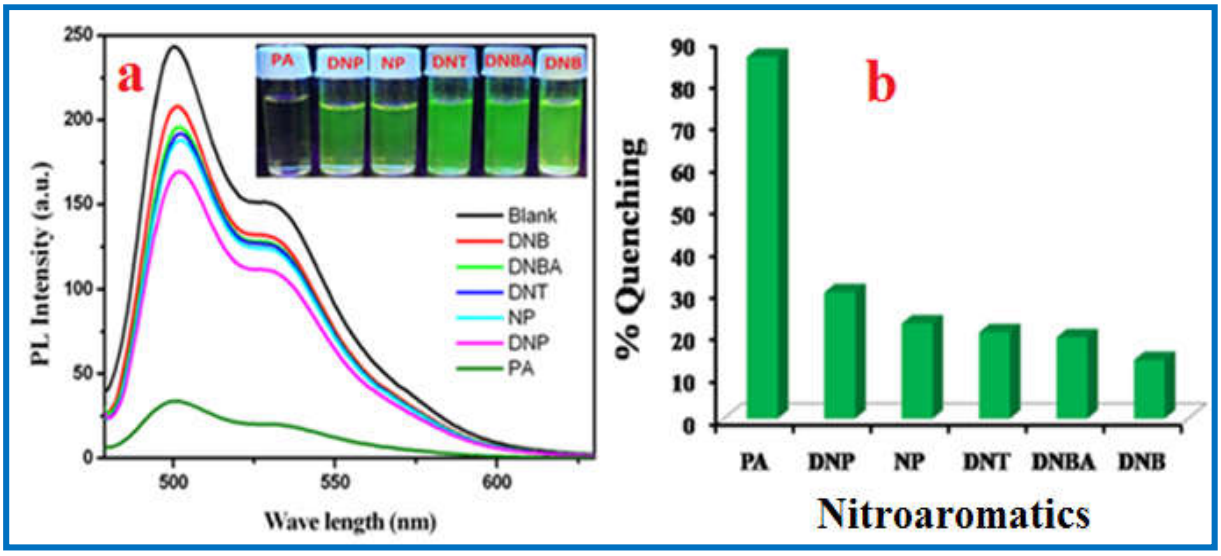

Fig. 5.16: a) Fluorescence emission spectra of $\mathbf{P^3}$ hydrosol (sample-d) in presence of fixed concentration (20 μM) of different nitro-derivatives (PA, DNP, NP, DNT, DNBA, DNB). Inset: Images of $\mathbf{P^3}$ hydrosol in presence of fixed concentration (20μM) of different nitroaromatics (PA, DNP, NP, DNT, DNBA, DNB) under illumination of 366 nm radiation. (b) Comparison of percentage fluorescence quenching of $\mathbf{P^3}$ hydrosol (sample-d) after the addition of fixed concentration (20μM) of various nitroaromatics.

Table 5.1: Stern-Volmer quenching constant (K_{SV} M^{-1}) for different nitroaromatics.

Nitro derivatives	R	K_{SV} (M^{-1})
PA	0.9930	1.9×10^5
DNP	0.9981	3.1×10^4
NP	0.9995	9.8×10^3
DNT	0.9967	9.1×10^3
DNBA	0.9975	8.7×10^3
DNB	0.9983	7.4×10^3

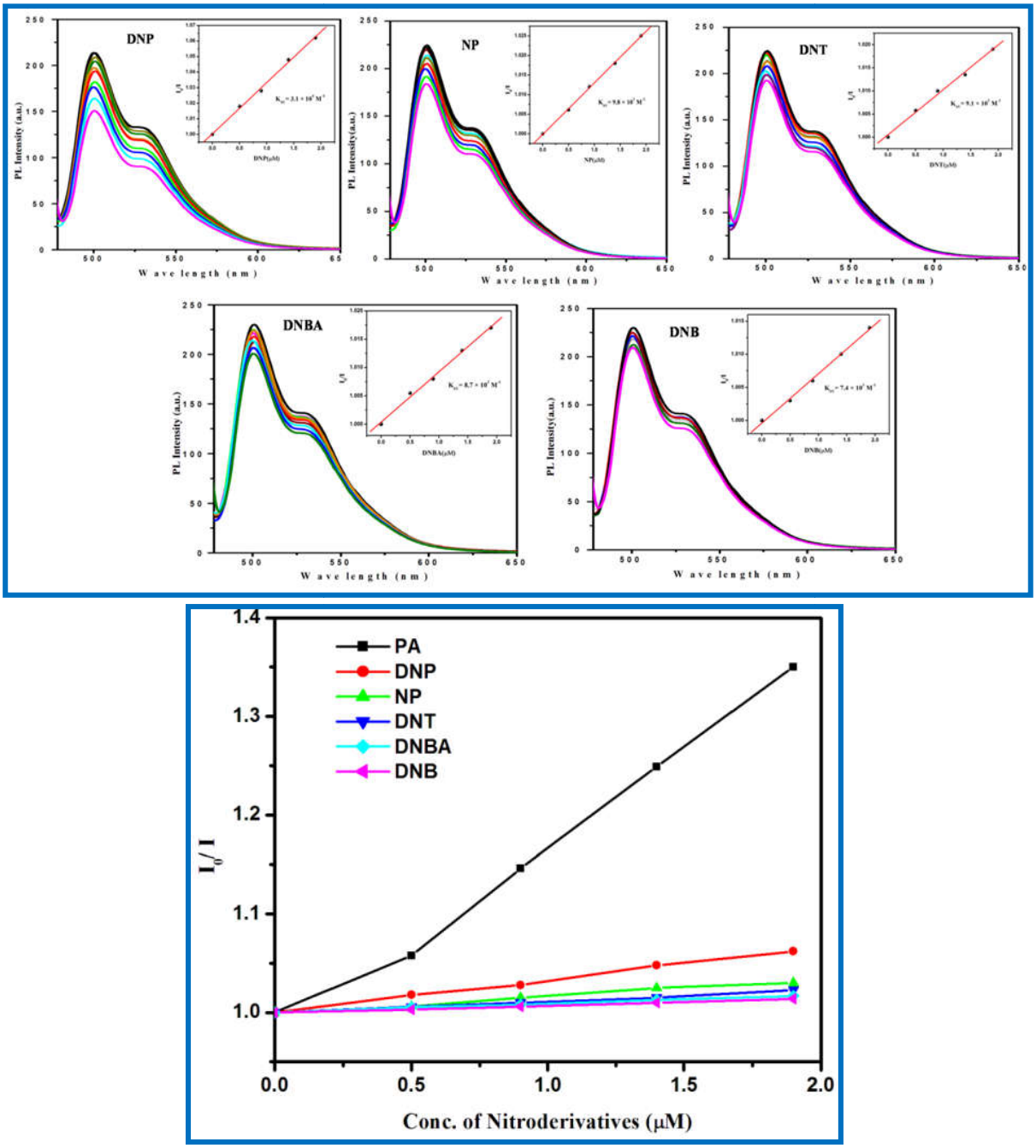

Fig. 5.17: Fluorescence Quenching of **P**[3] hydrosol in presence of picric acid (PA) 2,4-dinitro-phenol (DNP), 4-nitro-phenol (NP), dinitro-tolune (DNT), dinitro-benzoic acid (DNBA), dinitro-benzene (DNB).

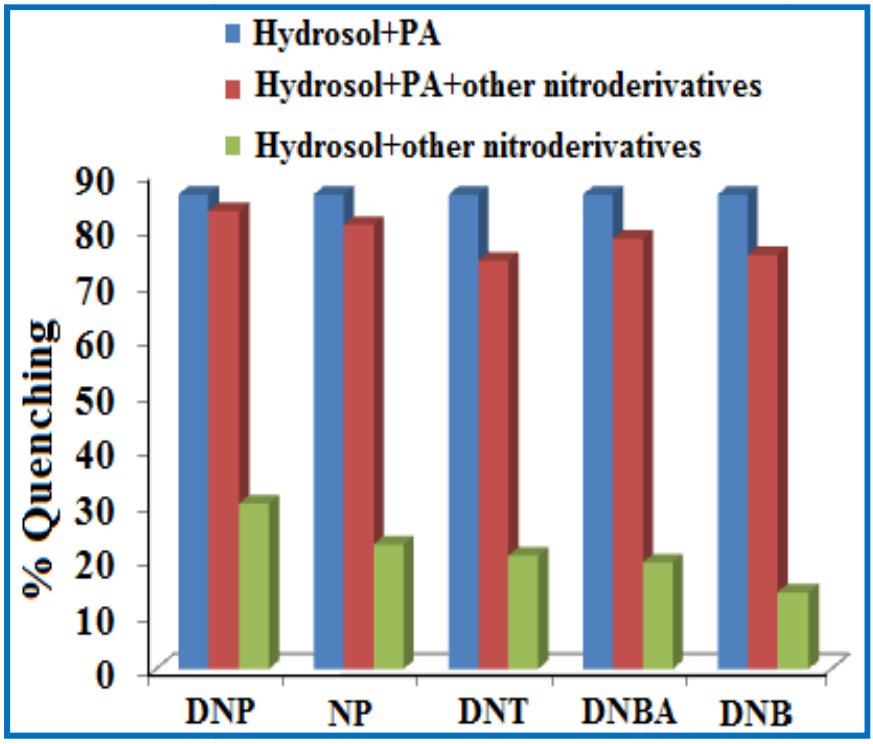

Fig. 5.18: Anti-interference experiment study of P^3 hydrosol.

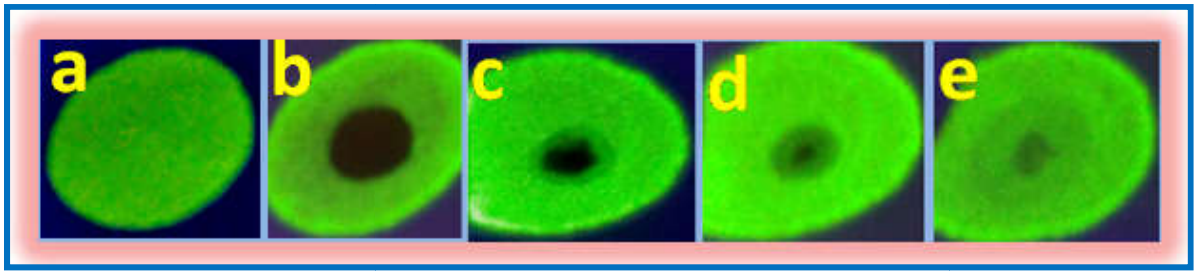

Fig. 5.19: Photographs (under illumination of 366 nm radiation) of fluorescence quenching of P^3 on test strips for the visual detection of small amount of PA (a) test strip without picric acid ; PA of different concentrations (b) 1×10^{-2} M, (c) 1×10^{-3} M, (d) 1×10^{-5} M, and (e) 1×10^{-7} M.

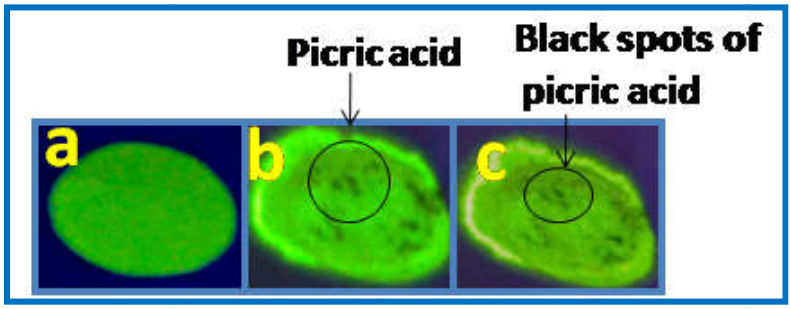

Fig. 5.20: Photographs (under illumination of 366 nm radiation) of P^3 on test strips (a) test strip without picric acid (b) picric acid crystal on test strip and (c) upon removal of picric acid crystals after 5 s.

5.4. Conclusion

In this work, we have synthesized through one step condensation process a simple fluorescence probe **P^3** (4-[(2-Hydroxy-naphthalen-1-ylmethylene)-amino]-1,5-dimethyl-2-phenyl-1,2-dihydro-pyrazol-3-one) which is weakly emissive in solution state, but it exhibits strong emission in its aggregated hydrosol showing aggregation induced emission enhancement (AIEE) properties. This emission behavior has been explained due to restriction of intramolecular rotation (RIR) and large amplitude vibrational modes of **P^3** in its aggregated state. Microstructures of **P^3** with various morphologies have been synthesized using reprecipitation method. The AIEE mechanism of **P^3** has been explained using UV–Vis absorption, steady state and time resolved spectroscopy. Computation of HOMO, LUMO electron densities of **P^3** reveals intramolecular charge-transfer between antipyrine and naphthalene group takes place upon photoexcitation. One more superb utility of this AIEE active molecule is its selective sensitivity towards picric acid (PA) with quenching constant 1.91×10^5 M^{-1}. It is further explained with the help of both steady state and time resolved emission study that the fluorescence quenching of **P^3** hydrosol in presence of PA takes place through static quenching mechanism.